


 Cite this: *RSC Adv.*, 2015, 5, 53259

Self-assembly formation of NiCo₂O₄ superstructures with porous architectures for electrochemical capacitors

 Ting Zhu,^a Zhen Yang Ang^b and Ghim Wei Ho^{*abc}

Nickel cobalt oxides (NiCo₂O₄) superstructures with microsized flowers (MF), nanoflowers (NF), nanoneedles (NN), and nanospheres (NS) have been prepared by a facile self-assembly formation and subsequent conversion process. The various morphologies of the nickel cobalt precursors (NCP) are tuned by using different salts, solvents, surfactants and reaction temperatures. The as-obtained NCP can be readily converted to NiCo₂O₄ through an annealing process with their structures well retained. The electrochemical properties of the as-derived NiCo₂O₄ are assessed as the active electrode materials. The results indicate that the NiCo₂O₄ has exhibited promising pseudo-capacitive properties with high capacitance and good cycling stability. The NF has delivered the highest specific capacitance of 636 F g⁻¹ (at a rate of 1 mV s⁻¹) among all the four samples, showing its potential application for next generation electrochemical capacitors.

Received 25th May 2015

Accepted 5th June 2015

DOI: 10.1039/c5ra09797e

www.rsc.org/advances

Introduction

The limited availability of fossil fuels and public concerns about conventional energy technologies have pushed the trend of research towards searching for renewable green energy resources, such as solar, tidal, geothermal and wind energy.^{1–5} In the past few years, green energy generation has been a hot research focus for the scientific community all over the world as traditional electricity generation method is bringing about a significant negative effect on our environment.^{6–8} It is one of the most pressing challenges scientists are facing nowadays but on the other hand is leading to a greater interest and demand in the development of novel materials for next-generation energy storage devices to capture energy resources.⁹ One of the most promising type of devices are supercapacitors, as known as electrochemical capacitors, which has the unique advantages including high-power capability and fast charge and discharge rates.¹⁰ They bridge the gap between batteries and conventional dielectric capacitors and gradually attract the attentions from the scientific community by providing higher energy density than conventional dielectric capacitors, and also longer cycling ability than normal batteries.^{11–13}

The surface charge storage does not require ionic diffusion within the electrode materials framework, and so generally

supercapacitors exhibit fast redox reaction rates but relatively lower energy density than batteries. As a result, many efforts in the scientific fields have been devoted to improve their electrochemical performances.^{13,14} The capacitances and cycling performances can be enhanced by developing porous and/or smaller size particles accompanied with high specific surface area.¹⁵

Some active materials with fabulous specific capacitance and redox reaction rates have drawn great attentions from the scientists such as MnO₂, NiO, Co₃O₄ and NiCo₂O₄. These transition metal oxides possess multiple oxidation states that exhibit excellent redox reaction rates and hence enhance the pseudocapacitive properties.^{16–24} As a binary metal oxide, NiCo₂O₄ is a low-cost and environmentally friendly metal combination that has a relatively higher electronic conductivity than single component metal oxides because of the redox contribution from both metals.^{25–28} The electrochemical performances of NiCo₂O₄ are reported to have a high dependence on the morphology.^{29–33} Feng *et al.* compiled various work on nickel based material and in their report.³⁴ Lou *et al.* reported spinel mesoporous NiCo₂O₄ nanosheets with a specific capacitance of 2010 F g⁻¹ at a scan rate of 2 mV s⁻¹.³⁵ Zou *et al.* synthesized 3D NiCo₂O₄ micro-sphere with specific capacitance of 1284 F g⁻¹ at 2 A g⁻¹ scan rate too.³⁶ In a report by Lei *et al.*, 3D hierarchical flower-shaped NiCo₂O₄ are fabricated with specific capacitance of 1006 F g⁻¹ at a scan rate of 1 A g⁻¹.³⁷ However, the morphologies exploration based on facile hydrothermal self-assembly process that is tunable to obtain different structured materials have not been well-explored. In this work, the different morphologies of NiCo₂O₄ leading to different electrochemical properties have been investigated. The as-

^aDepartment of Electrical and Computer Engineering, National University of Singapore, 4 Engineering Drive 3, Singapore 117583. E-mail: elehgw@nus.edu.sg

^bEngineering Science Programme, National University of Singapore, 9 Engineering Drive 1, Singapore 117575

^cInstitute of Materials Research and Engineering, A*STAR (Agency for Science, Technology and Research), 3 Research Link, 117602, Singapore

Table 1 Synthetic scheme of the NCP products

	Ni(Ac) ₂ ·4H ₂ O (g)	Co(Ac) ₂ ·4H ₂ O (g)	Urea (g)	SDS (g)	Solvent (20 mL)	Temperature
Micro-flowers	0.125	0.25	0	0	EtOH : water : PEG = 2 : 2 : 1	180 °C for 6 h
Nano-needles	0.125	0.25	0.5	0	EtOH : water = 9 : 1	90 °C for 12 h
Nano-flowers	0.125	0.25	0	0.1	EtOH : water = 1 : 1	90 °C for 12 h
Nano-spheres	0.05	0.1	0	0	IPA	180 °C for 6 h

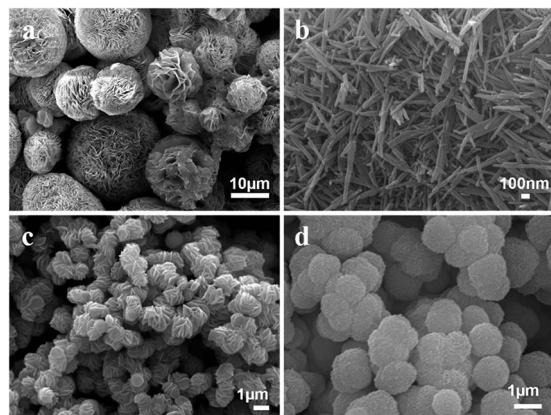
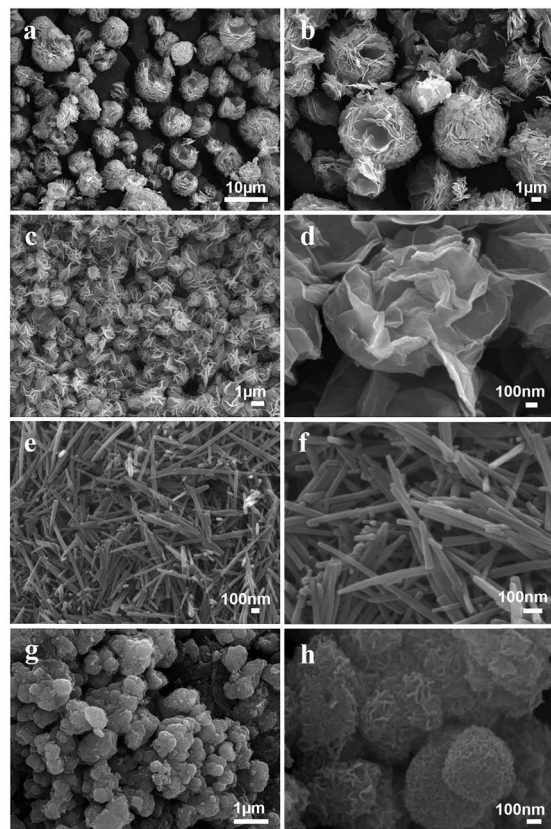


Fig. 1 FESEM images of the NCP with different morphologies: MF (a), NN (b), NF (c), and NS (d).

Fig. 2 FESEM images of the NiCo₂O₄ with different morphologies: MF (a and b), NF (c and d), NN (e and f), and NS (g and h).

derived porous and unique materials are used as electrode materials in supercapacitors, where the sample NF exhibits the best performance among all the samples.

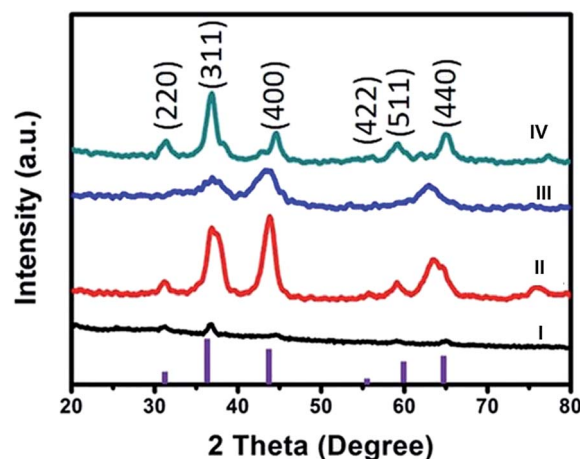
Experimental

Material preparation

The NCP can be synthesized by a simple hydrothermal process. In a typical synthesis of NCP for NF, metal acetate tetrahydrates with molar ratio of Ni/Co (1 : 2) was dissolved in a mixture of solvent consists of ethanol and water (20 mL, v/v = 1 : 1) at room temperature, subsequent by the addition of 0.1 g sodium dodecyl sulfate (SDS). The solution was then transferred to a 50 ml Teflon-lined stainless steel autoclave and heated at 90 °C for 12 hours. The resulting precursor was then harvested *via* centrifugation and rinsed with water and ethanol for a few times to remove excessive reactants before dried in air overnight. The synthesis of the NCP has been listed in Table 1. The NCP were then converted to NiCo₂O₄ by calcination in air at 300 °C for 2 h with a heating rate of 1 °C min⁻¹.

Materials characterization

The morphologies of samples were characterized by scanning electron microscopy (FESEM, JEOL FEG JSM-7001F) equipped with an energy dispersive X-ray spectroscopy (EDX), the X-ray diffraction (XRD, Philips X-ray diffractometer, Cu K α) and the transmission electron microscopy (TEM, Philips FEG CM300 equipped with selected area electron diffraction (SAED)).

Fig. 3 XRD patterns of the as-derived NiCo₂O₄ samples: MF(i), NF(ii), NN(iii) and NS(iv).

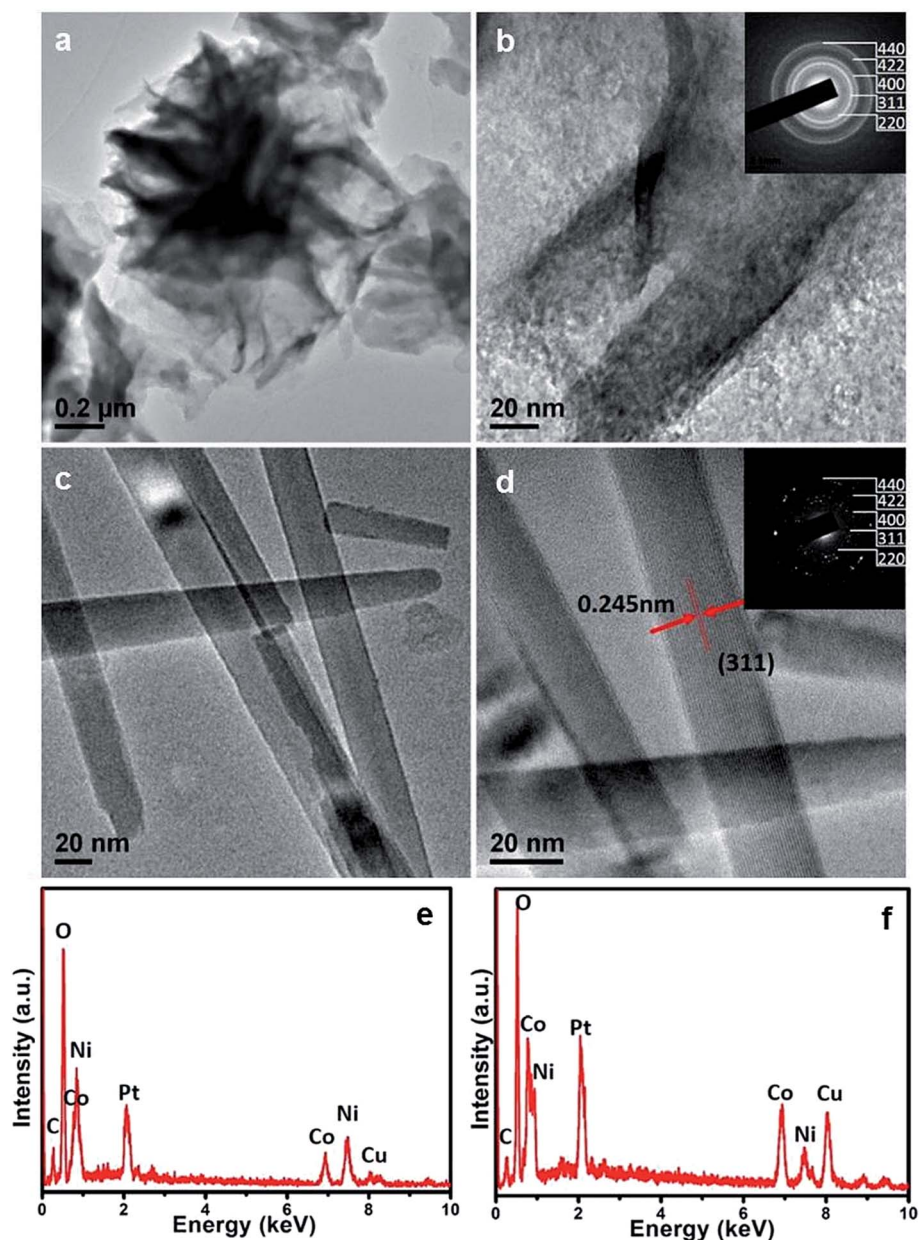


Fig. 4 TEM images (a–d) and EDX patterns (e and f) of NF (a, b and e) and NN (c, d and f).

Quantachrome NOVA-1200 system was used to measure the N_2 adsorption and desorption isotherms at 77 K. The BET (Brunauer–Emmett–Teller) surface area was obtained from the adsorption data where the relative pressure (P/P_0) ranging from 0.05 to 0.3.

Electrochemical measurements

The working electrodes were prepared by mixing the 80 wt% of electroactive material ($NiCo_2O_4$), 10 wt% of carbon black, and 10 wt% of polyvinylidene difluoride (PVDF, Aldrich). The slurry was then pressed onto metal Ni foams, and dried thoroughly at 60 °C. The electrolyte used was a 2 M of KOH aqueous solution. The electrochemical performances of the samples were evaluated on a CHI 660D electrochemical workstation using cyclic

voltammetry and chronopotentiometry tests with a three-electrode cell where Pt foil serves as the counter electrode and a standard calomel electrode (SCE) as the reference electrode.

Results and discussion

The synthesis for NCP is listed in Table 1. Sample MF is the calcined product of the corresponding NCP which was synthesized in a mixture of ethanol (EtOH), water (H_2O) and poly ethylene glycol (PEG) with volume ratio of 2 : 2 : 1. Changing the solvents to EtOH and water with volume ratio of 9 : 1 in the presence of urea as precipitator resulted in NN structures. EtOH : H_2O at 1 : 1 (volume) with addition of 0.1 g SDS has altered the morphology into NF, while the synthesis of NS NCP

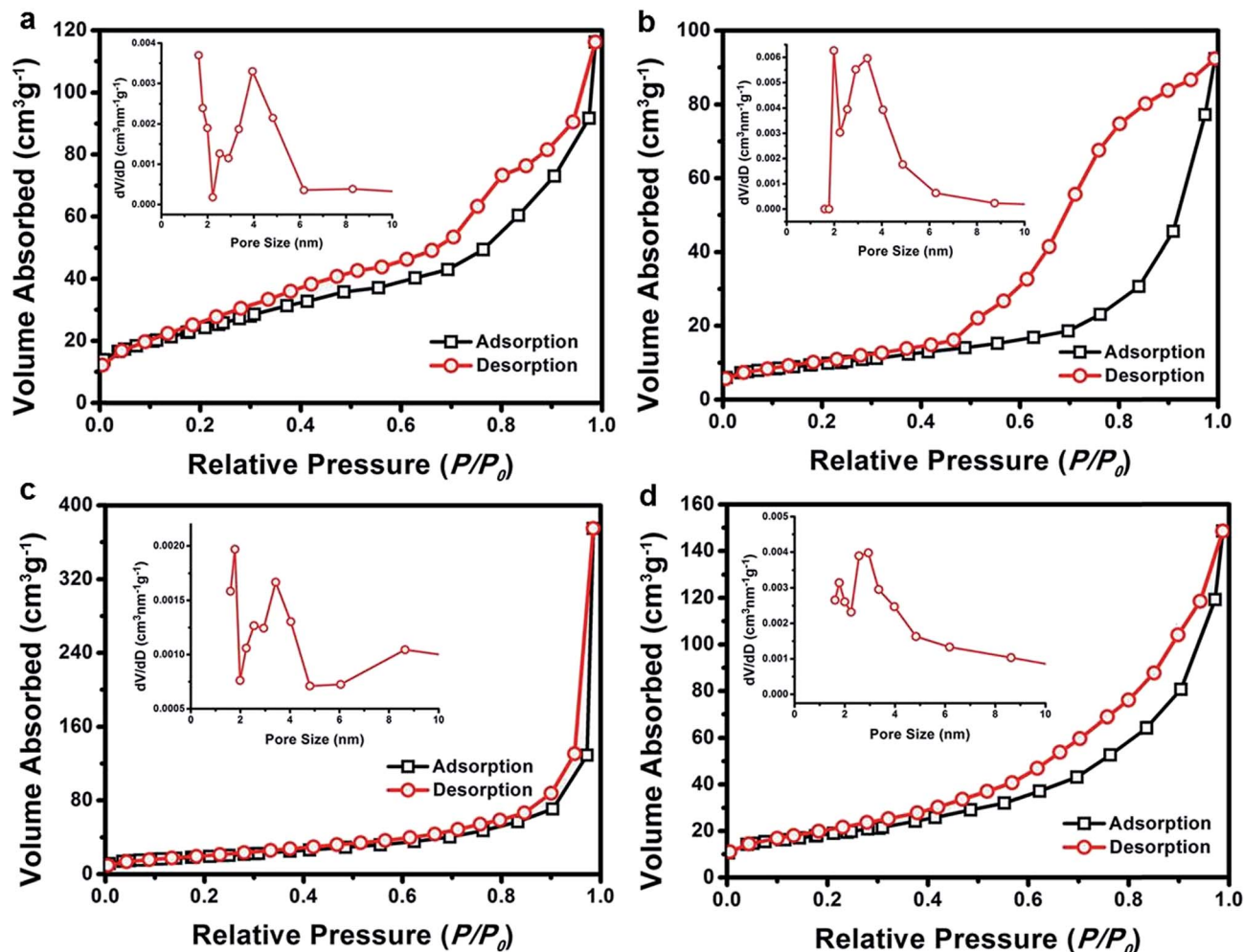


Fig. 5 BET results of NiCo₂O₄ samples MF (a), NF (b), NN (c) and NS (d). The insets show the corresponding pore size distributions, respectively.

used isopropanol (IPA) solely as the solvent without any additives. The as-prepared NCPs can be readily converted into NiCo₂O₄ by heat treatment in air.

Fig. 1 shows the FESEM images of all the NCP synthesized from different reaction conditions and surfactants. Fig. 1a was observed to present interconnected micro size sphere-like flower structures with diameters up to 10 μm. Fig. 1b presents needle-head nanorods with over 1 μm in length and 50 nm in width. Nanoflower-like structures are obtained by changing the volume ratio of ethanol and water in the presence of SDS (Fig. 1c). When the solvent was changed to sole IPA, we are able to produce the nanospheres with porous surfaces (Fig. 1d). It should be noted that the reaction during the hydrothermal synthesis is quite complicated due to the different solvents and surfactants used. The various morphologies appeared in the final products are the results by co-effect of solvents and surfactants. It is plausible that the solvents and surfactants have been served as the soft templates for the growth of NCP with different structures.

NiCo₂O₄ can be obtained by annealing the as-formed NCP samples at 300 °C for 2 hours in air to remove impurities and

defects in lattice structures. Fig. 2 shows the FESEM images of all the four NiCo₂O₄ samples. The microsized flower-like structures (MF) have been well retained after calcination (Fig. 2a and b), which shows the robustness of the structures. It can be observed that the nanoflower (NF) particles are composed of ultrathin nanosheets with morphologies well preserved after heat treatment (Fig. 2c and d). Some broken nanoneedles (NN) have been seen in Fig. 2e and f, which may be due to the high aspect ratios of the structure. The porous NS clusters have no significant change after the calcination except some agglomerations after combustion (Fig. 2g and h). The as-obtained NiCo₂O₄ samples were then examined by XRD (Fig. 3) in order to obtain the crystallographic details. All the indexed peaks can be attributed to (111), (220), (311), (400), (422), (511) and (440) planes of the cubic NiCo₂O₄ (JCPDS 73-1702).³⁸ No peaks of impurities have been found in the samples, which reveals the complete conversion of the NCP to the nickel cobalt oxides. The lowest crystallinity of MF sample can be observed among all the four samples, and this could be due to the largest particle sizes of MF, which makes it difficult for the heat

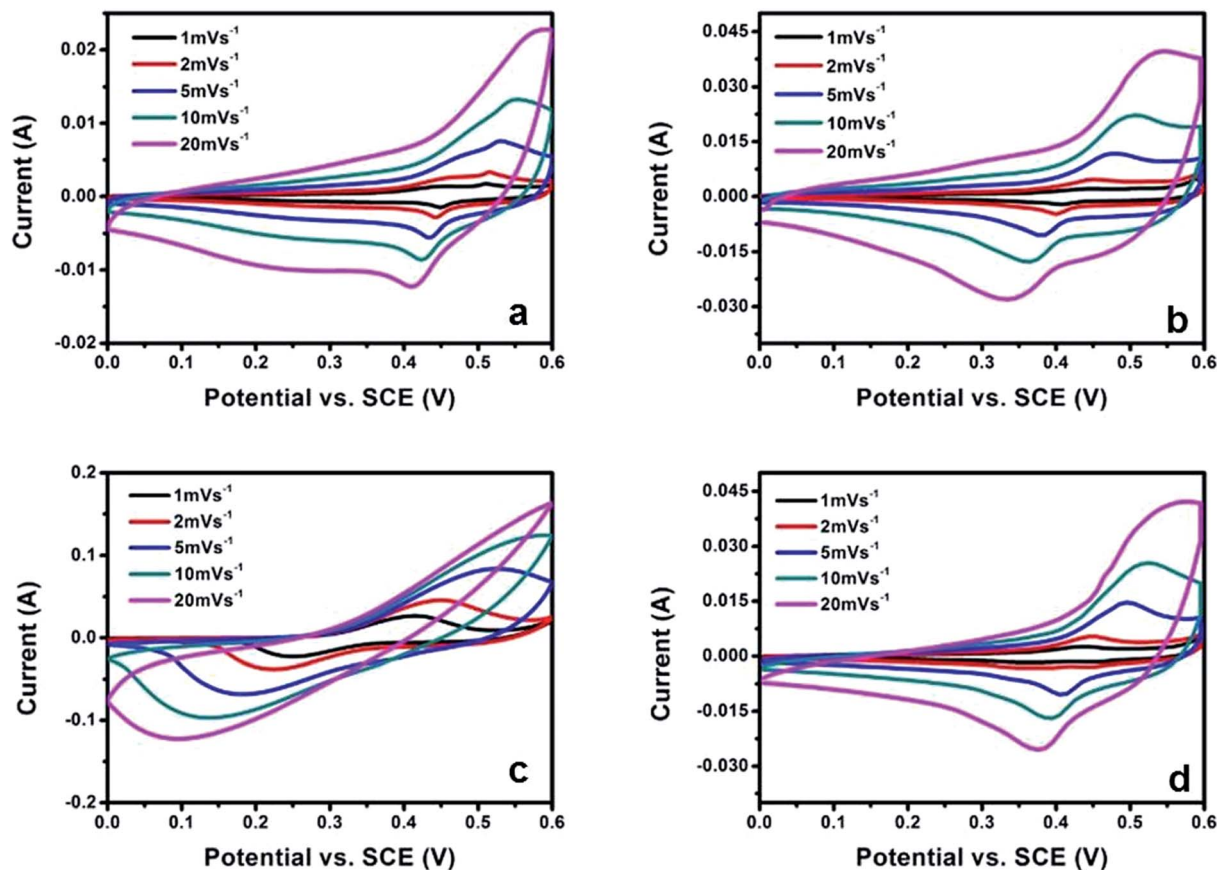


Fig. 6 CV curves of NiCo_2O_4 samples performed at different scan rates: MF (a), NN (b), NF (c) and NS (d).

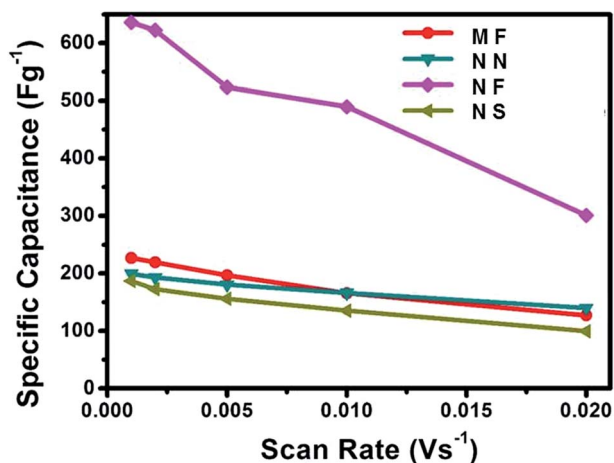


Fig. 7 Specific capacitances of NiCo_2O_4 samples calculated from CV curves with different scan rates.

treatment to achieve a high crystallinity at the same calcination temperature.

In order to further study the morphology of the as-obtained NiCo_2O_4 , the NF and NN samples were selected for the TEM characterization (Fig. 4). The NF sample is revealed to be composed of ultrathin nanosheets (Fig. 4a) with porous texture

seen in Fig. 4b, which is consistent with the previous FESEM findings (Fig. 2d). The NN sample is observed to have a uniform rod-like body and a sharp tip (Fig. 4c). Its higher resolution TEM image (HR-TEM) presents the fringes with a spacing of 2.45 Å that can be attributed to the (311) plane of NiCo_2O_4 .^{38,39} Both of the two samples are verified to be polymorph due to their circular structures from the SAED pattern (insets in Fig. 4b and d). Furthermore the EDX patterns shown in Fig. 4e and f indicate the presence of Ni and Co elements in the oxides, which has further strengthened the XRD results in Fig. 3. It should be noted that the presence of Cu and Pt peaks is attributed to that the EDX was performed on Cu substrate and the samples had been sputtered by Pt to further improve their electrical conductivity in order to obtain a clearer FESEM images.

The porous textural characteristics of the NiCo_2O_4 samples were examined by BET at 77 K. Fig. 5 shows the N_2 adsorption-desorption isotherms of all the four samples and their corresponding pore size distributions obtained from respective desorption branches are displayed as insets. These type IV isotherms possess small hysteresis loops observed at a relative pressure of 0.4–1 for Sample MF (a), NF (b), and NN (c) and 0.8–1 for NS (d) with a similar pore size distribution around 3–5 nm (insets). The BET specific surface areas of MF, NN, NF and NS are determined to be 58, 73, 95 and 89 $\text{m}^2 \text{g}^{-1}$, respectively. It can be noted that NF shows the highest surface area

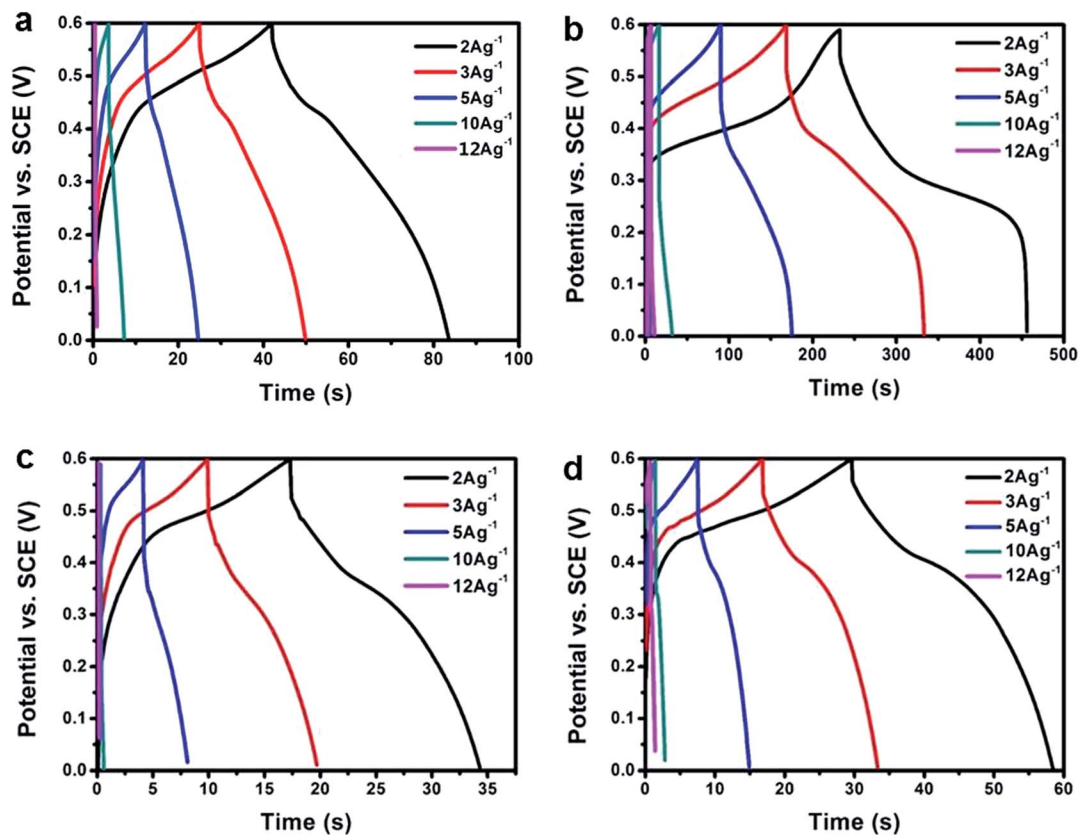


Fig. 8 Charge-discharge curves of the NiCo₂O₄ samples: MF (a), NF (b), NN (c) and NS (d).

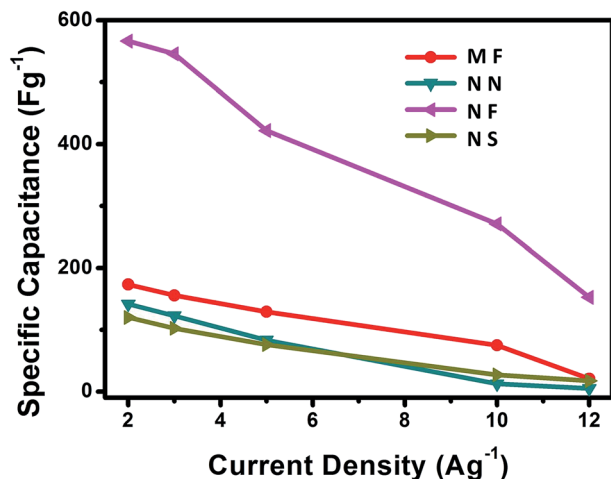


Fig. 9 Specific capacitances of NiCo₂O₄ samples calculated from discharge curves.

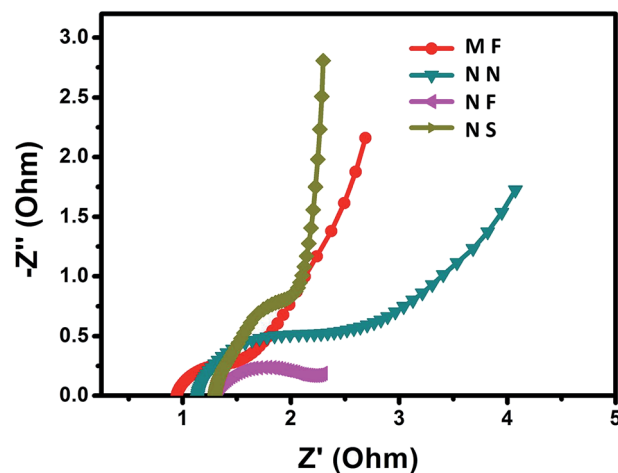


Fig. 10 EIS plots of the NiCo₂O₄ samples.

than all the other samples, which could provide more channels for the access of hydrated electrolyte ions.⁴⁰ These porous NiCo₂O₄ materials are then used as active materials for supercapacitor electrodes, where the electrochemical performances have been evaluated and compared.

Fig. 6 illustrates the CV curves performed at different scan rates (1, 2, 5, 10, 20 mV s⁻¹) with potential window ranging from

0 to 0.6 V (vs. SCE). Distinct redox peaks occurred at 0.3–0.45 V and 0.4–0.55 V can be observed clearly, which reveals the pseudocapacitive property of the electrodes. The different CV shapes of sample NF could be attributed to the different content of polarization of the electrode materials.⁴¹ The relevant redox reactions can be described as the following equation:^{42,43}



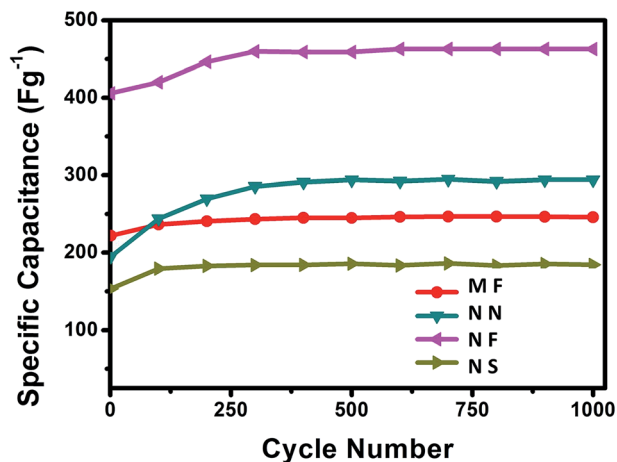


Fig. 11 Cycling performances of the NiCo_2O_4 samples.

The specific capacitances can be calculated by the following equation:

$$C = \frac{1}{2m \frac{dV}{dt} (V_a - V_b)} \int_{V_b}^{V_a} I(V) dV$$

where m is the active material mass, $\frac{dV}{dt}$ is the scan rate, $V_a - V_b$ represents the potential window which is 0.6 V and the last integral term is the area bounded by the CV curves.⁴⁴ Fig. 7 shows the comparison of specific capacitance of each sample at different scan rates. It is obvious to see that the NF shows extremely prominent specific capacitances of 636, 622, 524, 490 and 301 F g^{-1} at scan rates of 1, 2, 5, 10 and 20 mV s^{-1} , respectively. Lower capacitances of 227, 220, 197, 181 and 175 F g^{-1} at the same scan rates are observed from NN, while the maximum capacitances of the other two samples are less than 250 F g^{-1} , which are much lower than that of the NF. The highest capacitance of NF should be credited to its high specific surface area which consists of porous texture and its small particle size. However, sample MF has a relatively bulky structures, which caused the electrolyte ions difficult to diffuse into the inner area of particles, causing the capacitance lower than that of NF.⁴⁵

The charge–discharge is also conducted with various current densities using the same potential windows for all the four samples (Fig. 8). The charge–discharge curves displayed have conformed the pseudocapacitive characteristics, which is consistent with the previous CV results. Fig. 9 presents the graph of specific capacitances delivered at different current densities (2, 3, 5, 10, 20 A g^{-1}). The highest specific capacitance among all the samples is delivered by the sample NF at current density of 2 A g^{-1} (566 F g^{-1}). While a much lower value at 173.75 F g^{-1} is recorded at the same current density for sample MF, which demonstrates the sample trend with CV results. The highest values for the other two samples are calculated to be less than 200 F g^{-1} , which shows poorer performance than the NF sample.

The highest capacitance of sample NF can also be revealed from the EIS result (Fig. 10). The internal resistance of the

samples can be calculated from the range where high frequency semicircle intercepts with the x axis. It can be observed that the semicircle at high frequency range of NF is smaller, which indicates their lower charge-transfer impedance than all the other samples. Meanwhile, NF has a relatively straight vertical line in the low frequency range, indicating their better capacitive behavior and lower diffusion impedance.⁴⁶

All the fabricated electrodes are also tested for prolonged cycles to evaluate the stability. The CV measurements were repeated for 1000 cycles (10 mV s^{-1}), and the capacitances calculated from the cycles were displayed in Fig. 11. There is no distinct capacitance decay for all the four samples, which can be credited to their good cycling ability. The slightly increase of the capacitance in the first few hundreds cycles can be observed from all the samples. This increase can be attributed to the porous texture of the samples. The high porosity surface has allowed the electrolyte ions to diffuse into the inner area *via* different sizes of porous channels, which will lead to the electrode activation process and hence the capacitances are observed to be increased in the first few hundreds cycles.¹⁹ Sample NF has exhibited the highest specific capacitance due to its porous surface and high specific surface area by larger amount of electroactive sites for the redox reactions.^{47,48} It should be noted that the Ni foam template will only contribute $\sim 1.2\%$ of the total capacitances of all the samples according to our control experiment, and this means majority of the capacitances are delivered from the electroactive materials.

Conclusion

Four types of NCP products with different morphologies were prepared by a simple hydrothermal route employing by different solvents and surfactants. NiCo_2O_4 are then obtained by calcination of NCP at 300 °C in air for 2 hours. When used as electrode materials for supercapacitors, the nanoflower-like NiCo_2O_4 sample exhibits the best electrochemical performance with high specific capacitance (636 F g^{-1} at 1 mV s^{-1}) and good cycling stability. This result has provided a general method to synthesize the nanostructured materials for the next generation low-cost and high-performance supercapacitors.

Acknowledgements

This work is supported by MOE R-263-000-B38-112 and A*star R-263-000-A96-305.

References

- 1 B. Zhao, J. Song, P. Liu, W. Xu, T. Fang, Z. Jiao, H. Zhang and Y. Jiang, *J. Mater. Chem.*, 2011, **21**, 18792–18798.
- 2 C. Liu, F. Li, L. P. Ma and H. M. Cheng, *Adv. Mater.*, 2010, **22**, E28–E62.
- 3 Y. Zhu, S. Murali, M. D. Stoller, K. Ganesh, W. Cai, P. J. Ferreira, A. Pirkle, R. M. Wallace, K. A. Cychoz and M. Thommes, *Science*, 2011, **332**, 1537–1541.
- 4 A. S. Aricò, P. Bruce, B. Scrosati, J.-M. Tarascon and W. Van Schalkwijk, *Nat. Mater.*, 2005, **4**, 366–377.

- 5 M. Winter and R. J. Brodd, *Chem. Rev.*, 2005, **105**, 1021.
- 6 Y. Wang and Y. Xia, *Adv. Mater.*, 2013, **25**, 5336–5342.
- 7 B. E. Conway, *J. Electrochem. Soc.*, 1991, **138**, 1539–1548.
- 8 R. Kötz and M. Carlen, *Electrochim. Acta*, 2000, **45**, 2483–2498.
- 9 Y. Zhang, M. Ma, J. Yang, C. Sun, H. Su, W. Huang and X. Dong, *Nanoscale*, 2014, **6**, 9824–9830.
- 10 A. Pandolfo and A. Hollenkamp, *J. Power Sources*, 2006, **157**, 11–27.
- 11 P. Simon and Y. Gogotsi, *Nat. Mater.*, 2008, **7**, 845–854.
- 12 Q. Lu, J. G. Chen and J. Q. Xiao, *Angew. Chem., Int. Ed.*, 2013, **52**, 1882–1889.
- 13 A. Izadi-Najafabadi, S. Yasuda, K. Kobashi, T. Yamada, D. N. Futaba, H. Hatori, M. Yumura, S. Iijima and K. Hata, *Adv. Mater.*, 2010, **22**, E235–E241.
- 14 Y. Chen, B. Qu, L. Hu, Z. Xu, Q. Li and T. Wang, *Nanoscale*, 2013, **5**, 9812–9820.
- 15 Y. Zhu, Z. Wu, M. Jing, H. Hou, Y. Yang, Y. Zhang, X. Yang, W. Song, X. Jia and X. Ji, *J. Mater. Chem. A*, 2015, **3**, 866–877.
- 16 C. Yuan, X. Zhang, L. Su, B. Gao and L. Shen, *J. Mater. Chem.*, 2009, **19**, 5772–5777.
- 17 F. Jiao, A. H. Hill, A. Harrison, A. Berko, A. V. Chadwick and P. G. Bruce, *J. Am. Chem. Soc.*, 2008, **130**, 5262–5266.
- 18 S. Ding, T. Zhu, J. S. Chen, Z. Wang, C. Yuan and X. W. D. Lou, *J. Mater. Chem.*, 2011, **21**, 6602–6606.
- 19 T. Zhu, J. S. Chen and X. W. Lou, *J. Mater. Chem.*, 2010, **20**, 7015–7020.
- 20 S. K. Meher and G. R. Rao, *J. Phys. Chem. C*, 2011, **115**, 15646–15654.
- 21 J. Liu, J. Jiang, M. Bosman and H. J. Fan, *J. Mater. Chem.*, 2012, **22**, 2419–2426.
- 22 R. Rakhi, W. Chen, D. Cha and H. Alshareef, *Nano Lett.*, 2012, **12**, 2559–2567.
- 23 Z. Li, Y. Mi, X. Liu, S. Liu, S. Yang and J. Wang, *J. Mater. Chem.*, 2011, **21**, 14706–14711.
- 24 M. Liu, W. W. Tjiu, J. Pan, C. Zhang, W. Gao and T. Liu, *Nanoscale*, 2014, **6**, 4233–4242.
- 25 G. Q. Zhang, H. B. Wu, H. E. Hoster, M. B. Chan-Park and X. W. D. Lou, *Energy Environ. Sci.*, 2012, **5**, 9453–9456.
- 26 L. Huang, D. Chen, Y. Ding, S. Feng, Z. L. Wang and M. Liu, *Nano Lett.*, 2013, **13**, 3135–3139.
- 27 Z. Q. Liu, K. Xiao, Q. Z. Xu, N. Li, Y. Z. Su, H. J. Wang and S. Chen, *RSC Adv.*, 2013, **3**, 4372–4380.
- 28 W. Ni, B. Wang, J. L. Cheng, X. D. Li, Q. Guan, G. F. Gu and L. Huang, *Nanoscale*, 2014, **6**, 2618–2623.
- 29 D. Zhang, H. Yan, Y. Lu, K. Qiu, C. Wang, Y. Zhang, X. Liu, J. Luo and Y. Luo, *Dalton Trans.*, 2014, 15887–15897.
- 30 L. Shen, Q. Che, H. Li and X. Zhang, *Adv. Funct. Mater.*, 2014, **24**, 2630–2637.
- 31 X. Yao, C. Zhao, J. Kong, D. Zhou and X. Lu, *RSC Adv.*, 2014, **4**, 37928–37933.
- 32 Z. Wang, Y. Zhang, Y. Li and H. Fu, *RSC Adv.*, 2014, **4**, 20234–20238.
- 33 X. Liu, S. Shi, Q. Xiong, L. Li, Y. Zhang, H. Tang, C. Gu, X. Wang and J. Tu, *ACS Appl. Mater. Interfaces*, 2013, **5**, 8790–8795.
- 34 L. Feng, Y. Zhu, H. Ding and C. Ni, *J. Power Sources*, 2014, **267**, 430–444.
- 35 C. Yuan, J. Li, L. Hou, X. Zhang, L. Shen and X. W. D. Lou, *Adv. Funct. Mater.*, 2012, **22**, 4592–4597.
- 36 R. Zou, K. Xu, T. Wang, G. He, Q. Liu, X. Liu, Z. Zhang and J. Hu, *J. Mater. Chem. A*, 2013, **1**, 8560–8566.
- 37 Y. Lei, J. Li, Y. Wang, L. Gu, Y. Chang, H. Yuan and D. Xiao, *ACS Appl. Mater. Interfaces*, 2014, **6**, 1773–1780.
- 38 L. Li, Y. Cheah, Y. Ko, P. Teh, G. Wee, C. Wong, S. Peng and M. Srinivasan, *J. Mater. Chem. A*, 2013, **1**, 10935–10941.
- 39 Q. Wang, B. Liu, X. Wang, S. Ran, L. Wang, D. Chen and G. Shen, *J. Mater. Chem.*, 2012, **22**, 21647–21653.
- 40 C. Largeot, C. Portet, J. Chmiola, P.-L. Taberna, Y. Gogotsi and P. Simon, *J. Am. Chem. Soc.*, 2008, **130**, 2730–2731.
- 41 G. Q. Zhang and X. W. Lou, *Adv. Mater.*, 2013, **25**, 976–979.
- 42 X. Liu, Y. Zhang, X. Xia, S. Shi, Y. Lu, X. L. Wang, C. Gu and J. Tu, *J. Power Sources*, 2013, **239**, 157–163.
- 43 X. Wang, X. Han, M. Lim, N. Singh, C. L. Gan, M. Jan and P. S. Lee, *J. Phys. Chem. C*, 2012, **116**, 12448–12454.
- 44 C. H. An, Y. J. Wang, Y. A. Huang, Y. A. Xu, C. C. Xu, L. F. Jiao and H. T. Yuan, *CrystEngComm*, 2014, **16**, 385–392.
- 45 T. Zhu, E. R. Koo and G. W. Ho, *RSC Adv.*, 2015, **5**, 1697–1704.
- 46 M. D. Stoller, S. Park, Y. Zhu, J. An and R. S. Ruoff, *Nano Lett.*, 2008, **8**, 3498–3502.
- 47 T. Zhu, Z. Wang, S. Ding, J. S. Chen and X. W. D. Lou, *RSC Adv.*, 2011, **1**, 397–400.
- 48 H. B. Wu, H. Pang and X. W. D. Lou, *Energy Environ. Sci.*, 2013, **6**, 3619–3626.